Volume 1 | Number 1 | Jan 2013 | Pages 1–100

PCCP

Physical Chemistry Chemical Physics
www.rsc.org/pccp

ROYAL SOCIETY OF CHEMISTRY

ROYAL SOCIETY OF CHEMISTRY

www.rsc.org/pccp

Page 1 of 11

Physical Chemistry Chemical Physics
CREATED USING THE RSC LaTeX PCCP ARTICLE TEMPLATE – SEE www.rsc.org/electronicfiles FOR DETAILS

Modeling the local potential at Pt nanoparticles in polymer electrolyte membranes

Mohammad Javad Eslamibidgoli, Pierre-Éric Alix Melchy, and Michael H. Eikerling[a]

We present a physical-analytical model for the potential distribution at Pt nanodeposits in a polymer electrolyte membrane (PEM). Experimental studies have shown that solid deposits of Pt in PEM play a dual role in radical-initiated membrane degradation. Surface reactions at Pt particles could facilitate the formation as well as the scavenging of ionomer-attacking radical species. The net radical balance depends on local equilibrium conditions at Pt nanodeposits in the PEM, specifically, their equivalent local electrode potential. Our approach utilizes a continuum description of crossover fluxes of reactant gases, coupled with the kinetics of electrochemical surface reactions at Pt nanodeposits to calculate the potential distribution. The local potential is a function of the PEM structure and composition, which is determined by PEM thickness, concentrations of H_2 and O_2, as well as the size and density distribution of Pt particles. Model results compare well with experimental data for the potential distribution in PEMs.

1 Introduction

Prospects of unrivaled energy conversion efficiency and correspondingly reduced greenhouse gas emissions drive the global push towards polymer electrolyte fuel cell (PEFC) technology in automotive applications. Cost-effective utilization of materials as well as their stability and cycle life in the operating cell remain major challenges that must be successfully addressed. The durability and longevity of PEFCs are strongly affected by structural degradation of component materials, among which the polymer electrolyte membrane (PEM) is of central importance. The PEM degradation problem is critical for PEFC stack in fuel cell buses that must operate for >20,000 hours.[1] PEMs are exposed to thermal and mechanical stressors, coupled with the chemical attack of weak bonds of ionomer molecules by radical species, primarily .H, .OH and .OOH[2–4]. Experimental studies linked chemical degradation of the membrane to the concentrations of these radical species[5,6]. Deposits of Pt-in-the-membrane (PITM) are a consequence of Pt dissolution in the cathode catalyst layer[7]. Mobile Pt ion complexes diffuse and migrate into the membrane. They form solid deposits by precipitation in the presence of H_2 and O_2, crossed over from anode and cathode, respectively. Solid Pt nanodeposits provide catalyst surface sites for processes involved in formation or scavenging of radicals. In addition, surface reactions at PITM could facilitate the decomposition or formation of H_2O_2. In the latter case, H_2O_2 thus formed could react at impurities such as Fe_2^+ to produce radicals[2,8]. The effect of PITM on the durability of the PEM is still un-

der debate. Rodgers *et al.* have observed a strong impact of the Pt density on the degradation of Pt-impregnated membranes[9]. Ohguri *et al.* have investigated the formation of .OH at Pt particles in the membrane[10]. In their work, .OH is detected at both the anode and the cathode side but the amount is much larger for the anode side. Ghassemzadeh *et al.* have observed that the chemical degradation rate was higher in the presence of Pt catalyst for a H_2-rich mixture of H_2 and O_2 (90% H_2, 2% O_2, 8% Ar) as compared to an O_2 -rich mixture (20% O_2, 2% H_2, 78% Ar)[11]. A similar trend was reported by Aoki *et al.*[12,13] and Ohma *et al.*[14]. Other researchers have observed severe membrane degradation in the presence of Pt particles[15–17]; it has also been found that PITM can enhance durability by deactivating radicals and H_2O_2[18–20]. Conditions such as low relative humidity, high temperature, and high cell voltage accelerate chemical degradation due to an increased formation of H_2O_2 in the cell[21–23].

The balance of competing processes depends on local conditions such as temperature and relative humidity as well as the structure and local chemical composition of the PEM. The local chemical composition of the PEM is determined by pH and by mole fractions of H_2 and O_2 provided at opposite membrane sides. Local values of H_2 and O_2 concentrations can be calculated for given transport properties, composition and thickness of the PEM. The same conditions also determine the size, shape and density distribution of Pt deposits in the PEM[24–27]. On the other hand, the formation of PITM has a feedback effect on concentrations of H_2 and O_2 as well as membrane humidification[17]. Moreover, the rates of catalytic surface processes depend on size and shape of Pt nanoparticle deposits[21,27–29]. Understanding the impact of PITM on

[a] *Department of Chemistry, Simon Fraser University, 8888 University Drive, Burnaby, BC, Canada, V5A1S6; E-mail: meikerl@sfu.ca*

the chemical degradation of the PEM thus involves a complex phenomenology of local conditions and structure of the PEM, as well as structure-dependent transport and reaction processes.

The local open circuit potential (OCP) of a Pt nanoparticle, considered as a nanoelectrode in the PEM, is determined by the conditions listed above. Liu and Zuckerbrod have measured the OCP distribution at a Pt nanoprobe in the membrane, with H_2 and air provided at opposite membrane sides[30]. They have observed a step-like potential profile. The local electrode potential in the region close to the anode was found near 0 V vs. RHE. In the region near the cathode, the OCP was found to attain values between 0.8 V and 1.0 V. Takaichi *et al.* have measured the OCP distribution determined by H_2 and O_2 permeation in the membrane. They have observed a change in the step position at different O_2 partial pressure and relative humidity[31]. Later, using the microprobe technique, Ohishi *et al.* have studied the distribution of the OCP[32]. They have investigated the influence of operating conditions on O_2 transport properties and the effect on the potential at the probe insertion position.

Understanding the problem of electrostatic potential at isolated metallic nanoparticles in an electrolyte is fundamentally interesting and of broader practical impact. Specifically, the problem of Pt nanodeposits in polymer electrolyte membranes has received significant attention in recent years. However, to the best of our knowledge only one modeling work has been devoted to this topic[33]. Atrazhev *et al.* have developed a model to predict the potential distribution at a single Pt particle in the PEM[33]. Their model employs an "ad hoc" formulation of the problem, in which the surface concentrations of reactant gases, H_2 and O_2, at a spherical Pt particle are obtained as functions of particle position. The relations are substituted in the Butler-Volmer equations and the charge balance condition is applied to numerically calculate the local mixed potential at the particle. Their model, however, suffers from physically inconsistent relations obtained for the current densities of hydrogen oxidation reaction (HOR) and oxygen reduction reaction (ORR), i.e. Eqs (36) and (37) in their paper[33]. As discussed in their paper, at the position of the potential step, both HOR and ORR are controlled by diffusion of reactant gases to the particle surface; thus, at this position, each of the current densities must be independent of the particle potential. However, in their relevant equations the dependency still exists. In addition, the implementation and parameterization of HOR and ORR kinetics employed in their model are incompatible with experimental data[34–36].

In this paper, we present a rigorous and self-consistent formulation of the problem which results in a physical-analytical model of the mixed-potential distribution at Pt nanodeposits in the PEM. The model employs continuum diffusion for the crossover of reactant gases, H_2 and O_2, coupled with local
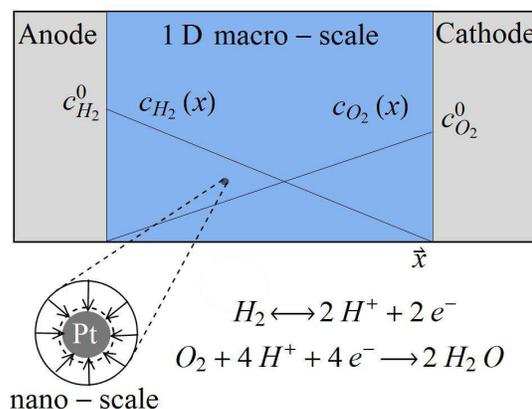

Fig. 1 Model representation of a Pt nanoparticle in the membrane. The model assumes macroscale diffusion of H_2 and O_2 from the opposite membrane boundaries, coupled with local diffusion around Pt nanodeposits and reactions (HOR and ORR) at the Pt surface.

electrochemical reactions at the surface of Pt nanoparticles. The analytical solution gives the shapes of reactant concentrations and potential profile in terms of experimental parameters, including the relative concentration of H_2 and O_2 at the PEM boundaries, mass transfer coefficients, kinetic parameters of surface reactions at Pt, and size and density of Pt particles in the PEM. Model outcomes are compared to experimental measurements of the OCP at Pt nanodeposits in the membrane[30,31].

2 The Model

The model incorporates a two-scale description of transport and reaction processes in the membrane, as illustrated in Fig. 1. At the macroscale, one-dimensional (1D) diffusion governs the distribution of redox species, i.e., H_2 and O_2, along the thickness variable x. Even though we do not consider the membrane embedded in the fuel cell configuration, we refer to the side at which hydrogen is supplied as the anode and the side at which oxygen is provided as the cathode. Concentrations of hydrogen and oxygen in the PEM are $c_{H_2}(x)$ and $c_{O_2}(x)$. The concentrations at the PEM boundaries are $c_{H_2}^0$ at $x = 0$ (anode side) and $c_{O_2}^0$ at $x = l$ (cathode side). At the nanoscale, the hydrogen oxidation reaction (HOR), $H_2 \leftrightarrow 2H^+ + 2e^-$, and the oxygen reduction reaction (ORR), $O_2 + 4H^+ + 4e^- \rightarrow 2H_2O$ proceed at the surface of Pt nanoparticles, which we assume spherical. As Pt nanoparticles are not connected to an electron source/sink, the resulting OCP must fulfill a condition that the rates of HOR and ORR processes are balanced at the particle level.

As shown in Fig. 2, four regimes can be distinguished to describe the mixed reaction kinetics at the surface of Pt nanode-
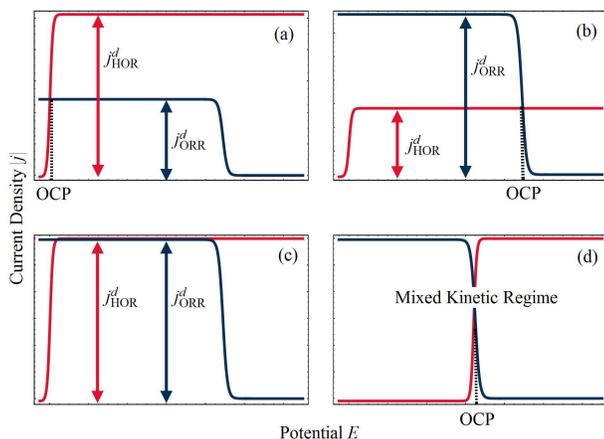
Fig. 2 Schematic representation of HOR and ORR polarization curves, indicating open circuit potential (OCP). Plots (a) and (b) correspond to mixed diffusion-kinetic regimes for HOR and ORR. For the situation depicted in (c) both reactions are limited by local diffusion, whereas in (d) both reactions are controlled by the kinetics of surface reactions.

posits in the PEM. The distinction is based on the comparison of diffusion and kinetically-limited current densities of HOR and ORR at the spherical Pt nanoelectrode. The diffusion limited current density of the HOR is[37]

$$j_{HOR}^{d} = 2F c_{H_2}(x) \frac{D_{H_2}^{nano}}{r_0}, \tag{1}$$

and that of the ORR is

$$j_{ORR}^{d} = 4F c_{O_2}(x) \frac{D_{O_2}^{nano}}{r_0}, \tag{2}$$

where F is the Faraday constant, r_0 is the Pt particle radius, $D_{H_2}^{nano}$ and $D_{O_2}^{nano}$ are the diffusion coefficients of H_2 and O_2 at the nanoscale, respectively.

For the faradaic current densities of HOR and ORR at the particle surface, we use expressions in the form of the Butler-Volmer equation, i.e.,

$$j_{HOR} = j_{HOR}^{0} \left(\left(\frac{c_{H_2}^{s}(x)}{C_{ref}} \right) \exp \left[\frac{\alpha_{HOR}^{a}}{b} E(x) \right] \right.$$
$$\left. - \exp \left[-\frac{\alpha_{HOR}^{c}}{b} E(x) \right] \right), \tag{3}$$

and

$$j_{ORR} = j_{ORR}^{0} \left(\left(\frac{c_{O_2}^{s}(x)}{C_{ref}} \right) \exp \left[-\frac{\alpha_{ORR}^{c}}{b} (E(x) - E^{eq}) \right] \right.$$
$$\left. - \exp \left[\frac{\alpha_{ORR}^{a}}{b} (E(x) - E^{eq}) \right] \right), \tag{4}$$

where $b = \frac{RT}{F}$, $c_{H_2}^{s}$ and $c_{O_2}^{s}$ are surface concentrations of H_2 and O_2, respectively, and $C_{Ref} = 40.88 \times 10^{-6} mol/cm^3$ is a reference concentration[38]. It corresponds to the O_2 concentration at standard conditions. α^a and α^c are the anodic and cathodic electron transfer coefficients, j_{HOR}^{0} and j_{ORR}^{0} are the exchange current densities of HOR and ORR, and E^{eq} is the equilibrium potential of ORR (vs. RHE). R and T are the gas constant and temperature, respectively.

For a Pt nanodeposit at position x, one of four possible scenarios will determine the local value of the OCP, $E(x)$: (1) If $j_{HOR}^{d} > j_{ORR}^{d}$, then the HOR is controlled by reaction kinetics and the ORR is diffusion-limited, as shown in Fig. 2 (a); in this case, $E(x)$ remains close to the equilibrium potential of the HOR. (2) If $j_{HOR}^{d} < j_{ORR}^{d}$, then the HOR is diffusion-limited and the ORR is kinetically controlled; in this case, $E(x)$ shifts towards the equilibrium potential of the ORR, as illustrated in Fig. 2 (b). (3) The transition between the two cases occurs at the position where $j_{HOR}^{d} = j_{ORR}^{d}$, as shown in Fig. 2 (c); in this regime, the current density at the particle is independent of $E(x)$; it corresponds to a step-like change in $E(x)$ at a position x_0. From the condition of equal diffusion-limited current densities in this regime, we will determine the value of x_0. (4) The last possible scenario is that both reactions are controlled kinetically, as depicted in Fig. 2 (d); in this case, $E(x)$ is found from the condition $j_{HOR} = j_{ORR}$, using Eqs. 3 and 4.

Following the distinction of different kinetic regimes, governing the local current at the nanoparticle surface, the PEM can be divided into two spatial regions, viz. an anodic region at $x < x_0$, in which $j_{HOR}^{d} > j_{ORR}^{d}$ and a cathodic region at $x > x_0$, in which $j_{HOR}^{d} < j_{ORR}^{d}$. In the anodic region, the HOR current is kinetically controlled, whereas the ORR is usually in the diffusion-limited regime. In the cathodic region, the ORR is kinetically controlled, whereas the HOR is usually in the diffusion-limited regime.

If a reaction at the Pt surface is kinetically controlled, the surface concentration of redox species will be equal to the bulk concentrations, i.e. $c_{H_2}^{s} = c_{H_2}(x)$ in the anodic region and $c_{O_2}^{s} = c_{O_2}(x)$ in the cathodic membrane region. For diffusion-limited reactions, we will assume zero surface concentration of the transport-limited reactant, i.e. $c_{O_2}^{s} \approx 0$ in the anodic region and $c_{H_2}^{s} \approx 0$ in the cathodic region. As we are interested in obtaining analytical solutions for the potential profile $E(x)$, we will employ modified forms of the Butler-Volmer expressions in Eqs. 3 and 4, given by

Physical Chemistry Chemical Physics Accepted Manuscript

$$j_{HOR} = 2j_{HOR}^0 \left(\frac{c_{H_2}(x)}{C_{ref}} \right) \sinh \left[\frac{1}{2b} E(x) \right], \qquad (5)$$

and

$$j_{ORR} = j_{ORR}^0 \left(\frac{c_{O_2}(x)}{C_{ref}} \right) \exp \left[-\frac{1}{b} (E(x) - E^{eq}) \right]. \qquad (6)$$

In Eqs. 5 and 6, we assume $\alpha_{HOR}^a = \alpha_{HOR}^c = \frac{1}{2}$ [34] and $\alpha_{ORR}^c = 1$ [35,36]. In Eq. 5 the sinh-expression for the faradaic current density of the HOR represents a common interpolation [39]. It allows for a continuous description of the HOR rate in the limit of small overpotential, $E(x) \leq b/3$, where $c_{H_2}(x) \approx C_{ref}$, and high overpotential, $E(x) \geq 3b$, where $2\sinh[E(x)/2b] \approx \exp[E(x)/2b]$. The single term BV-equation for the ORR in Eq. 6 is the standard form, accounting for the irreversible kinetics of the ORR.

We apply the charge balance condition for anodic and cathodic regions in the PEM and at the transition between these regions, to obtain analytical relations for the potential profile. In the anodic region, i.e. for $x < x_0$, we have

$$j_{HOR} = j_{ORR}^d. \qquad (7)$$

Inserting Eqs. 2 and 5 and solving for $E(x)$ results in

$$E(x) = 2b \sinh^{-1} \left[\frac{1}{2} \frac{c_{O_2}(x)}{c_{H_2}(x)} \frac{J_{ORR}^d}{j_{HOR}^0} \right] \qquad (8)$$

with

$$J_{ORR}^d = 4FC_{ref} \frac{D_{O_2}^{nano}}{r_0}. \qquad (9)$$

Similarly, in the cathodic region of the PEM, i.e. for $x > x_0$, we have

$$j_{ORR} = j_{HOR}^d. \qquad (10)$$

In this case, using Eqs. 1 and 6 and solving for $E(x)$, gives

$$E(x) = E^{eq} - b \ln \left[\frac{c_{H_2}(x)}{c_{O_2}(x)} \frac{J_{HOR}^d}{j_{ORR}^0} \right] \qquad (11)$$

with

$$J_{HOR}^d = 2FC_{ref} \frac{D_{H_2}^{nano}}{r_0}. \qquad (12)$$

At $x = x_0$, both the current densities of HOR and ORR are controlled by diffusion and, therefore,

$$j_{HOR}^d = j_{ORR}^d, \qquad (13)$$

which leads to a unique relation between the ratio of the bulk concentrations of the reactant gases at x_0, and the diffusion coefficients,

$$2c_{O_2}(x_0) D_{O_2}^{nano} = c_{H_2}(x_0) D_{H_2}^{nano}. \qquad (14)$$

Eq. 14 can be solved to find x_0 whence the distributions $c_{O_2}(x)$ and $c_{H_2}(x)$ are known.

The last possible case is when both current densities of HOR and ORR are controlled by reaction kinetics,

$$j_{HOR} = j_{ORR}. \qquad (15)$$

In this scenario, the potential profile is obtained using Eqs. 5 and 6, giving,

$$E(x) = 2b \ln \left[\frac{12^{1/3} + \left(\kappa(x) + \sqrt{(\kappa(x))^2 - 12} \right)^{2/3}}{18^{1/3} \left(\kappa(x) + \sqrt{(\kappa(x))^2 - 12} \right)^{1/3}} \right], \qquad (16)$$

where

$$\kappa(x) = 9 \left(\frac{c_{O_2}(x)}{c_{H_2}(x)} \frac{j_{ORR}^0}{j_{HOR}^0} \right) \exp \left[\frac{E^{eq}}{b} \right]. \qquad (17)$$

Eqs. 8, 11 and 16 allow expressing the potential profile in the PEM through the distribution of concentrations, $c_{H_2}(x)$ and $c_{O_2}(x)$. In order to obtain the concentrations, we must solve 1D diffusion equations for hydrogen and oxygen in the distinct PEM regions.

We define $\xi = \frac{x}{l}$ as the dimensionless coordinate along the membrane thickness and $\xi_0 = \frac{x_0}{l}$ as the dimensionless position of the potential step. In the anodic region ($\xi < \xi_0$), the reaction-diffusion equation for O_2 is

$$\frac{d^2 c_{O_2}(\xi)}{d\xi^2} = \Lambda^{-2} c_{O_2}(\xi), \qquad (18)$$

and that for H_2, using Eq. 7, is

$$\frac{d^2 c_{H_2}(\xi)}{d\xi^2} = \frac{2\Lambda^{-2}}{\delta^2} c_{O_2}(\xi), \qquad (19)$$

with

$$\delta^2 = \frac{D_{H_2}^{macro}}{D_{O_2}^{macro}} \qquad (20)$$

and

$$\Lambda = \frac{1}{l} \left(4\pi r_0 n_{Pt} \left(\frac{D_{O_2}^{nano}}{D_{O_2}^{macro}} \right) \right)^{-1/2}, \qquad (21)$$

where n_{Pt} is the number of Pt particles per unit PEM volume. The product Λl represents the dimensional reaction penetration depth of O_2. In the dilute limit of Pt particle distributions $\Lambda \gg 1$, and in the dense limit $\Lambda \ll 1$.

The diffusion coefficients at nanoscale and macroscale are distinguished as the structure and effective transport resistance of the medium is different at the two scales. The macroscale diffusion coefficient corresponds to diffusion in a random composite medium, with randomly mixed resistances due to polymer and water-filled domains. Nanoscale diffusion coefficients, on the other hand, approach the values for water. Therefore, the macroscopic diffusion coefficient will be smaller than the value in water by a factor that incorporates percolation effects. We consider this value as 10 because the diffusion coefficient of H_2 and O_2 in water[40] is one order of magnitude larger than its value in Nafion. This ratio is included in Λ in Eq. 21.

Due to large overpotential for the ORR at the anode, we assume that O_2 is completely used up at $\xi=0$. The boundary conditions of Eqs. 18 and 19 are given by

$$c_{O_2}(\xi = 0) = 0, c_{O_2}(\xi_0) = c_{O_2}^{\xi_0}, \tag{22}$$

and

$$c_{H_2}(\xi = 0) = c_{H_2}^0, c_{H_2}(\xi_0) = c_{H_2}^{\xi_0}. \tag{23}$$

The solution of Eqs. 18 and 19 subject to the boundary conditions 22 and 23 are as follows,

$$c_{O_2}(\xi) = c_{O_2}^{\xi_0} \frac{\sinh(\Lambda^{-1}\xi)}{\sinh(\Lambda^{-1}\xi_0)}, \tag{24}$$

$$c_{H_2}(\xi) = \frac{2}{\delta^2} c_{O_2}^{\xi_0} \frac{\sinh(\Lambda^{-1}\xi)}{\sinh(\Lambda^{-1}\xi_0)} + \left(c_{H_2}^{\xi_0} - c_{H_2}^0 - \frac{2}{\delta^2}c_{O_2}^{\xi_0}\right)\frac{\xi}{\xi_0} + c_{H_2}^0. \tag{25}$$

Similarly, in the cathodic region of the PEM ($\xi > \xi_0$), the reaction-diffusion equation of H_2 is

$$\frac{d^2 c_{H_2}(\xi)}{d\xi^2} = \Lambda^{-2} c_{H_2}(\xi), \tag{26}$$

and that of O_2, using Eq. 10, is

$$\frac{d^2 c_{O_2}(\xi)}{d\xi^2} = \frac{\Lambda^{-2}\delta^2}{2} c_{H_2}(\xi). \tag{27}$$

Here, for simplicity, we assume $\left(\frac{D_{O_2}^{nano}}{D_{O_2}^{macro}}\right) = \left(\frac{D_{H_2}^{nano}}{D_{H_2}^{macro}}\right)$, so that Λ is the same as defined in Eq. 21.

The boundary conditions are

$$c_{H_2}(\xi_0) = c_{H_2}^{\xi_0}, c_{H_2}(\xi = 1) = 0, \tag{28}$$

and

$$c_{O_2}(\xi_0) = c_{O_2}^{\xi_0}, c_{O_2}(\xi = 1) = c_{O_2}^0. \tag{29}$$

The solutions of Eqs. 26 and 27 are

$$c_{H_2}(\xi) = c_{H_2}^{\xi_0} \frac{\sinh(\Lambda^{-1}(\xi - 1))}{\sinh(\Lambda^{-1}(\xi_0 - 1))}, \tag{30}$$

$$c_{O_2}(\xi) = \frac{\delta^2}{2} c_{H_2}^{\xi_0} \frac{\sinh(\Lambda^{-1}(\xi - 1))}{\sinh(\Lambda^{-1}(\xi_0 - 1))} + \left(c_{O_2}^{\xi_0} - c_{O_2}^0 - \frac{\delta^2}{2}c_{H_2}^{\xi_0}\right)\frac{\xi - 1}{\xi_0 - 1} + c_{O_2}^0. \tag{31}$$

To obtain the equations for $c_{H_2}^{\xi_0}$ and $c_{O_2}^{\xi_0}$, we apply the continuity condition at $\xi = \xi_0$,

$$\frac{dc_{H_2}(\xi)}{d\xi}\Big|_{\xi=\xi_0^-} = \frac{dc_{H_2}(\xi)}{d\xi}\Big|_{\xi=\xi_0^+};$$
$$\frac{dc_{O_2}(\xi)}{d\xi}\Big|_{\xi=\xi_0^-} = \frac{dc_{O_2}(\xi)}{d\xi}\Big|_{\xi=\xi_0^+}. \tag{32}$$

Inserting Eqs. 25 and 30, we obtain

$$\left(\frac{2\Lambda^{-1}\xi_0}{\delta^2}\coth\left(\Lambda^{-1}\xi_0\right) - \frac{2}{\delta^2}\right)c_{O_2}^{\xi_0} = \left(\Lambda^{-1}\xi_0\coth\left(\Lambda^{-1}(\xi_0 - 1)\right) - 1\right)c_{H_2}^{\xi_0} + c_{H_2}^0. \tag{33}$$

Similarly, by inserting Eqs. 24 and 31 into Eq. 32, we obtain

$$\left(\frac{\Lambda^{-1}\delta^2(\xi_0 - 1)}{2}\coth\left(\Lambda^{-1}(\xi_0 - 1)\right) - \frac{\delta^2}{2}\right)c_{H_2}^{\xi_0} = \left(\Lambda^{-1}(\xi_0 - 1)\coth\left(\Lambda^{-1}\xi_0\right) - 1\right)c_{O_2}^{\xi_0} + c_{O_2}^0. \tag{34}$$

Eqs. 33 and 34 are solved to obtain $c_{H_2}^{\xi_0}$ and $c_{O_2}^{\xi_0}$ (see Appendix for the solutions). In the dilute limit of Pt particles, as $\Lambda \gg 1$, $c_{H_2}^{\xi_0} = c_{H_2}^0(1-\xi_0)$ and $c_{O_2}^{\xi_0} = c_{O_2}^0\xi_0$.

Substituting the relations for $c_{H_2}^{\xi_0}$ and $c_{O_2}^{\xi_0}$, obtained in the Appendix, into Eq. 14 the position of the potential step is found as

$$\xi_0 = \frac{1}{1 + \frac{2}{\delta^2}\frac{c_{O_2}^0}{c_{H_2}^0}}. \tag{35}$$

It indicates that as the uniform distribution of particles is assumed, ξ_0 is independent of the size and density of particles and only depends on the relevant concentrations of reactant

gases at boundaries and the ratio of diffusion coefficients. This result is independent of the particle shape. The effect of particle shape appears in the form of the diffusion limited current densities and as well in Λ. ξ_0 is obtained by applying the charge balance condition for the limiting current densities of HOR and ORR as given in Eq. 13. In this equation, as the parameters affecting the particle shape are assumed to be the same for HOR and ORR, they cancel out from both sides of the equation for any particle shape. In addition, for a uniform distribution the step position is independent of Λ, hence of the particle shape.

2.1 Model parameters

Physical properties and constants are listed in Table 1. The adopted values for the macroscale diffusion coefficients correspond to H_2 and O_2 diffusion in Nafion® 117, evaluated at 100% RH and 60°C[41]. Exchange current densities of the HOR and ORR have been extracted from Refs. (42) and (36), respectively.

As the molar concentrations of H_2 and O_2 in Nafion are reasonably small for the relevant partial pressures, we use Henry's law to relate H_2 and O_2 concentrations at the membrane boundaries to external partial pressures,

$$c_{H_2}^0 = H_{H_2} p_{H_2}^0 \; ; \; c_{O_2}^0 = H_{O_2} p_{O_2}^0. \tag{36}$$

with Henry's law constants H_{H_2} and H_{O_2} in Nafion. Substituting Eq. 36 into Eq. 35, we obtain

$$x_0 = \frac{l}{1 + 2\beta \frac{p_{O_2}^0}{p_{H_2}^0}}, \tag{37}$$

where

$$\beta = \frac{D_{O_2}^{\text{macro}} H_{O_2}}{D_{H_2}^{\text{macro}} H_{H_2}}. \tag{38}$$

The value of β used in this work is taken from Ref. (25). It is reported as 0.38 ± 0.05, evaluated experimentally in permeability tests of crossover hydrogen and oxygen at 100% RH and 65°C[25].

The evaluated ranges of parameters are listed in Table 2. The ranges correspond to values of parameters reported in the literature. As a baseline for parametric studies, we consider a membrane with $l = 50 \; \mu m$ in which particles with $r_0 = 150$ nm are uniformly distributed with $n_{Pt} = 5 \times 10^9 \; cm^{-3}$. The range of n_{Pt} is estimated based on the amount of Pt in the membrane. Results of electron microscopy-energy dispersive spectroscopy analysis have been used to quantify the amount of Pt transported from cathode to the membrane[25]. This study estimates that $\approx 13\%$ of Pt in the cathode is transported into the membrane following 3000 potential cycles. This amount

Table 1 Physical parameters, symbols and values

Description	Value	Ref.
Faraday constant, F	$96485 \; C/mol$	
Gas constant, R	8.314 J/mol K	
Temperature, T	$333 \; K$	
ORR equilibrium potential, E^{eq}	$1.23 \; V$	
Reference H_2 molar concentration, C_{ref}	$40.88 \times 10^{-6} \; mol/cm^3$	38
Reference O_2 molar concentration, C_{ref}	$40.88 \times 10^{-6} \; mol/cm^3$	38
H_2 diffusion coefficient in Nafion, $D_{H_2}^{macro}$	$1.2 \times 10^{-5} \; cm^2/s$	41
O_2 diffusion coefficient in Nafion, $D_{O_2}^{macro}$	$2.1 \times 10^{-6} \; cm^2/s$	41
HOR exchange current density, j_{HOR}^0	$0.8 \times 10^{-3} \; A/cm^2$	42
ORR exchange current density, j_{ORR}^0	$5.4 \times 10^{-11} \; A/cm^2$	36
Transfer coefficients for HOR, $\alpha_{HOR}^a = \alpha_{HOR}^c$	1/2	34
Transfer coefficient for ORR, α_{ORR}^c	1	35

Table 2 Ranges for parameters

Description	Value
H_2 pressure at membrane|anode, $p_{H_2}^0$, kPa	21-125
O_2 pressure at membrane|cathode, $p_{O_2}^0$, kPa	21-125
Particle radius, r_0, nm	50-5000
Membrane thickness, l, μm	25-200
Particle density, n_{Pt}, cm^{-3}	10^7-10^{10}

corresponds to $\approx 0.38 \; mg$ Pt, if we consider a Pt loading of 0.1 $mg \; cm^{-2}$ for a $5 \times 5 \; cm$ membrane. Equivalently, this amount results in a uniform distribution of Pt particles with $r_0 = 150$ nm and $n_{Pt} \approx 10^{10} \; cm^{-3}$ across a membrane with $l = 50 \; \mu m$.

3 Results and discussion

Fig. 3 shows the concentration profiles of H_2 and O_2 across the PEM and the step position, ξ_0, in dilute and dense limit of Pt particles. As shown, the position of ξ_0, given by Eq. 35 (or 37), depends on the relative concentrations of reactant gases at the membrane boundaries. The step shifts towards the cathode as $p_{H_2}^0$ increases relative to $p_{O_2}^0$ and vice versa. In the uniform particle distribution regime, ξ_0 is independent of Λ, as can be seen from Eq. 37.
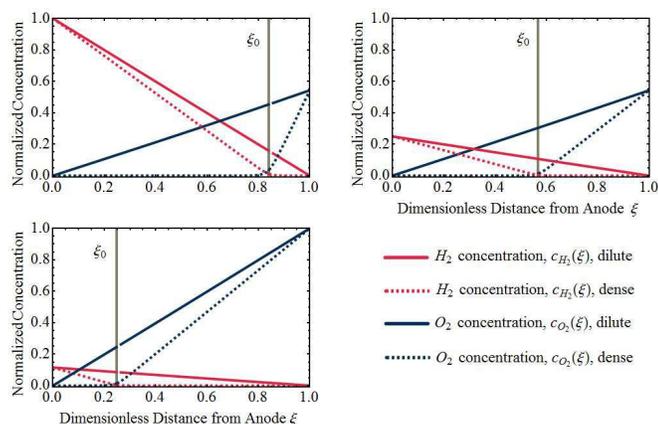
Fig. 3 Analytical solution of concentration profiles of H_2 and O_2 in dilute limit ($\Lambda \gg 1$) and dense limit ($\Lambda \ll 1$) of uniformly distributed Pt deposits for various relative concentrations of H_2 and O_2 at the PEM boundaries. The position of potential step, ξ_0, is indicated as vertical dashed line which is independent of particle density.

Fig. 4 Potential distribution at spherical Pt nanodeposits in the PEM. The graphs shown in (a) to (c) illustrate change in the local reaction regime with increasing size of the Pt nanoelectrode.

As shown in Fig. 3, in the dilute limit of Pt particles, as $\Lambda \gg 1$, the concentration profiles are linear, given by $c_{H_2}(\xi) = c_{H_2}^0(1-\xi)$ and $c_{O_2}(\xi) = c_{O_2}^0\xi$ (see Eqs. 24, 25, 30 and 31). As $\Lambda \to 1$ concentration profiles deviate from linear curves. According to Eq. 18 and 19, nonlinearity occurs when the local rate of reactant consumption is of similar order of magnitude as the rate of reactant flux. In dense limit, as $\Lambda \ll 1$, both concentrations approach to zero at ξ_0 which is expected as a trivial solution to Eq. 14.

For the case of a dense Pt band formed in the PEM, due to the small rate of transport and high rate of consumption at the position of the dense Pt layer, the concentration of reactants must approach to zero at the band position. In this case, the potential step is found to occur in the vicinity of the band, which is in agreement with experiment[25]. The particle deposition process in the membrane is due to repeated oxidation/dissolution and reduction/deposition of the migrated Pt ions by crossover O_2 and H_2, respectively[28]. At x_0 optimal conditions are provided for the deposition of particles to form the Pt band.

Fig. 4 shows the potential distribution at spherical Pt particles in the PEM for a uniform distribution with $n_{Pt} = 10^{10}$ cm^{-3}. In Fig. 4 (a)-(c), the potential profile in the mixed kinetic regime (see Fig. 2 (d) and Eq. 16) is compared to those of mixed "kinetic-diffusion" regimes in the two PEM regions (see Fig. 2 (a), Fig. 2 (b), Eq. 8 and Eq. 11). The results indicate that for particles with radius smaller than $r_0 \approx 125$ nm, the transition of ORR from diffusion-limited to kinetically controlled regime occurs at $\xi < \xi_0$. Similarly, for this particle size range, the transition of HOR from diffusion-limited to kinetically controlled regime occurs at $\xi > \xi_0$. In the re-
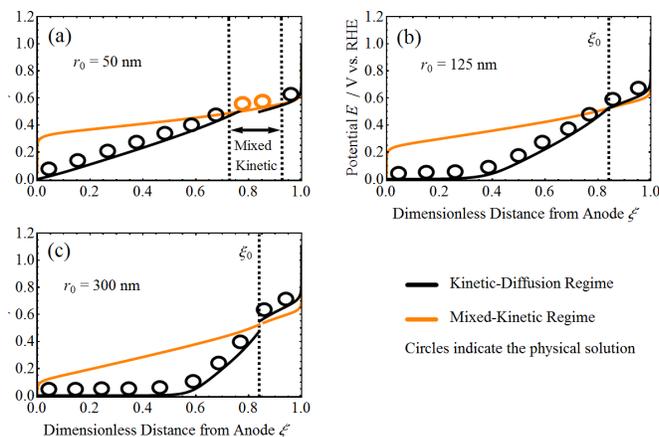
gion between the two dashed lines in Fig. 4 (a), both HOR and ORR are controlled by the reaction kinetics. This case is more relevant to the Pt in the membrane, as the average PITM sizes reported in the literature are smaller than 125 nm[43,44]. It implies that in the vicinity of the potential step the concentration gradient of the reactants close to the particle surface is negligible as both reactions are kinetically controlled. On the other hand, for particles with radius greater than $r_0 \approx 125$ nm the transition occurs at ξ_0, as shown in Fig. 4 (b) and (c) (also see Fig. 2 (c) and Eq. 14).

In Fig. 5 (a), the potential profile is plotted as a function of the particle size at a particle density of $n_{Pt} = 5 \times 10^9$ cm^{-3}, for a membrane with thickness of $l = 50$ μm. As shown, the OCP depends on the particle size, especially close to the step. As the particle size increases the potential decreases in the anodic region and increases in the cathodic region. The OCP change as a function of microelectrode size has been experimentally reported[45]. Particle size dependence of potential has also been obtained in the model by Atrazhev *et al.*[33].

Fig. 5 (b), shows the potential profile for a constant particle size (150 nm) as a function of n_{Pt}. As n_{Pt} increases, the potential decreases in anodic region and increases in the cathodic region. For a constant particle size and uniform particle distribution, as the PEM thickness increases the potential decreases in the anodic region and increases in the cathodic region, as shown in Fig. 5 (c). At ξ_0, the value of the potential drop only depends on the particle size. At this position, the ratio of the concentrations of reactant gases is independent of the particle density (see Eq. 14); thus, according to Eqs. 8 and 11 the potential drop is independent of n_{Pt}.

Fig. 6 shows the current density distribution at Pt nanoparticles in the PEM as a function of particle density, corresponding to the potential distribution shown in Fig. 5 (b). At $\xi < \xi_0$,
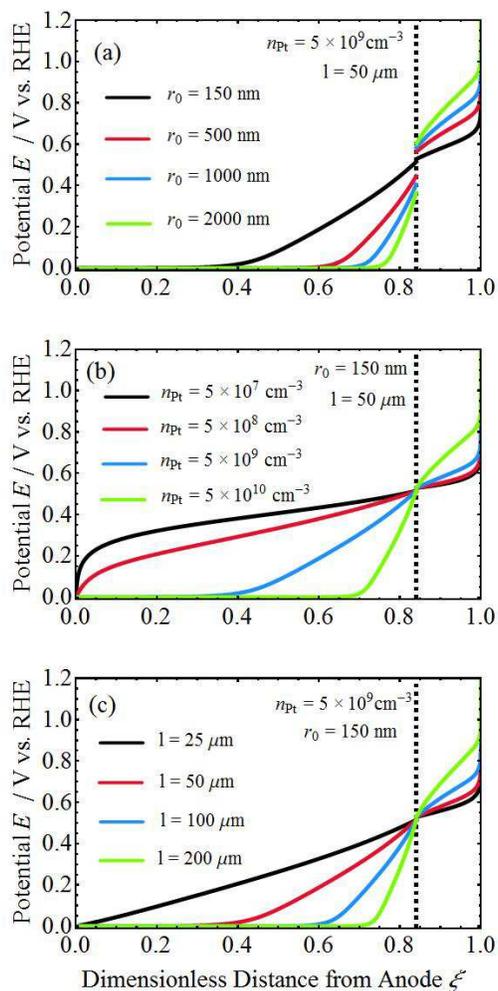
Fig. 5 Analytical solution of the potential distribution at spherical Pt nanodeposits in membrane, for (a) varying particle sizes, (b) varying particle densities, and (c) varying membrane thickness.

the current density increases from zero to a maximum value at ξ_0 (see Eq. 2); and at $\xi > \xi_0$ the current density decreases to zero (see Eq. 1). As n_{Pt} increases, the local flux becomes smaller due to the higher consumption of crossover gases.

Fig. 7 compares the model and experimental data of the potential profile for various relative partial pressures of H_2 and O_2. In the experimental measurements of Takaichi *et al.*[31], seven Pt microelectrode probes, with 30 μm in diameter, were used to measure the OCP determined by H_2 and O_2 permeating in the PEM. The microelectrodes are sandwiched between eight thin membrane films, 25 μm Nafion® (NRE211, Dupont, 3 × 7 cm), resulting in the total thickness of about 200 μm. H_2 at ambient pressure was fed to the anode side. At the cathode side, O_2 was held at partial pressures of 21 kPa, 25 kPa, 101 kPa and 119 kPa. In the experimental measurements per-
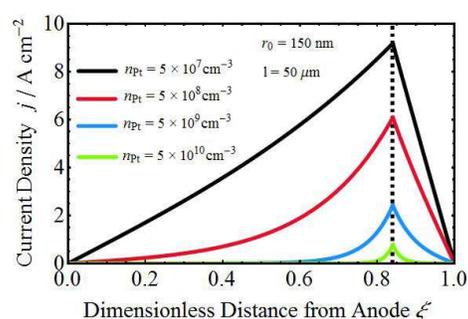

Fig. 6 Current density distributions at spherical Pt nanoelectrode calculated in the model, for various values of the particle density, corresponding to the cases depicted in Fig. 5b.

formed by Liu and Zuckerbrod[30], flattened Pt wires with an initial diameter of 25 or 50 μm were used. Two Pt microelectrodes were laminated within a membrane electrode assembly with a dimension of 5 × 5 cm. Three layers of membranes were used. Two 10 μm GORE-SELECT® (GSM) membranes sandwiched a membrane with variable thickness, X. The two microelectrodes were laminated in between the outer 10 μm GORE-SELECT membrane and membrane X, both aligned with the gas inlet region, one close to the cathode and the other close to the anode. The position of the microelectrode area the cathode side was varied by changing the thickness of the membrane X. Both anode and cathode were standard GORE-PRIMEA® Series 5510 electrodes with Pt loadings of 0.4 mg/cm^2. H_2 and air under 100 kPa pressure was fed to the anode and cathode sides, respectively. The potential at the microelectrodes was measured under OCP conditions at 60 °C.

To compare our model with the experimental data, we assume a spherical Pt microelectrode with r_0=5 μm in a membrane with $l = 200$ μm and a dilute particle density of $n_{Pt} = 10^7$ cm^{-3}. For the H_2 partial pressure we assumed 100 kPa and for the O_2 partial pressure we used the values reported in experiment. The variation in microelectrode shape does not demand a modification of the model; it is merely a parametric effect in the diffusion-limited current densities at the particle surface[37]. We use Eq. 37 to determine x_0 with $\beta = 0.38$ for all the pressure settings.

The potential shapes calculated from the model are in a very good agreement with values of the potential found in experiment. As shown in Fig. 7, the step-like potential profile is very well reproduced in the model and the dependence of the position of the step to relative partial pressures at the membrane boundaries is captured. Discrepancies might be due to a combination of the effect of microelectrode size and shape. Microelectrodes used in the experiments are large compared to the thickness of the membrane; hence, the spatial localiza-
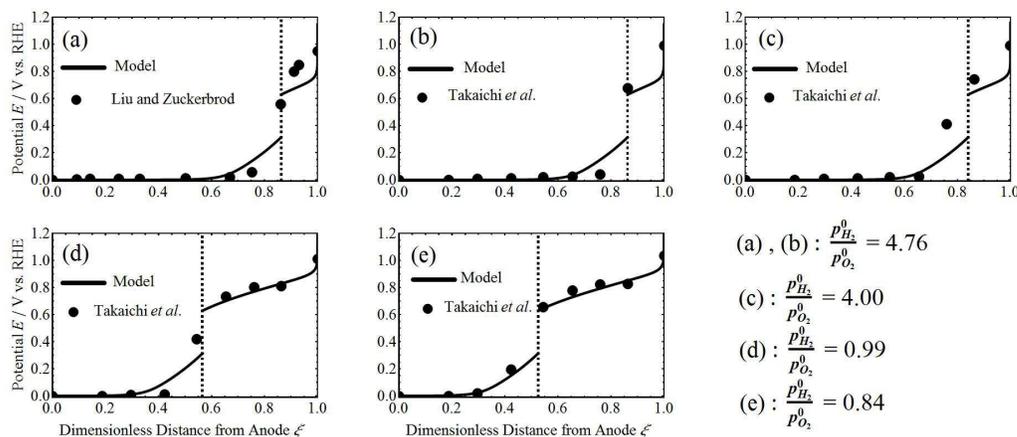
Fig. 7 Comparison between potential distributions and those observed in experiment [30,31] for various relative partial pressures of H_2 and O_2 at the membrane boundaries, as indicated in the graphs. Parameters used in calculations are listed in Table 1 and 2.

tion of potential values is relatively imprecise and represents effective values. In contrast, the model predicts the exact local value of the potential at a spherical microelectrode in the PEM. It is required to perform experimental studies with smaller microelectrodes in order to obtain better spatial resolution.

4 Conclusions

We presented an analytical model to determine the potential distribution at spherical Pt nanodeposits in the polymer electrolyte membrane. The approach incorporates a continuum description of crossover fluxes of reactant gases at the macroscale, coupled with the kinetics of electrochemical surface reactions at Pt nanodeposits. The potential distribution is obtained as a function of the local composition of the PEM, which is given by concentrations of H_2 and O_2 as well as the size and density distribution of Pt particles. In good agreement with experimental data, the model predicts a step-like potential profile. In the anodic region of the PEM, the potential is close to the equilibrium potential of the HOR. In the cathodic region, the potential is closer to the equilibrium potential of the ORR. For a uniform distribution of Pt particles, the position of the step is only determined by the relative partial pressures of H_2 and O_2 at the membrane interfaces as well as their permeation properties in the PEM. In the future we will use this model to rationalize the balance of degrading species involved in chemical degradation of polymer electrolyte membranes.

5 Appendix

In this appendix, the solution of Eqs. 33 and 34 for $c_{H_2}^{\xi_0}$ and $c_{O_2}^{\xi_0}$ are presented. Rewriting the Eqs. 33 and 34,

$$\mathcal{R} c_{H_2}^{\xi_0} = \mathcal{S} c_{O_2}^{\xi_0} + \mathcal{T} \; ; \; \mathcal{U} c_{H_2}^{\xi_0} = \mathcal{V} c_{O_2}^{\xi_0} + \mathcal{W} \qquad (39)$$

$c_{H_2}^{\xi_0}$ and $c_{O_2}^{\xi_0}$ are given by:

$$c_{H_2}^{\xi_0} = \frac{\mathcal{S}\mathcal{W} - \mathcal{T}\mathcal{V}}{\mathcal{U}\mathcal{S} - \mathcal{R}\mathcal{V}}, \; ; \; c_{O_2}^{\xi_0} = \frac{\mathcal{R}\mathcal{W} - \mathcal{T}\mathcal{U}}{\mathcal{U}\mathcal{S} - \mathcal{R}\mathcal{V}}. \qquad (40)$$

where,

$$\mathcal{R} = \Lambda^{-1}\xi_0 \coth\left[\Lambda^{-1}(\xi_0 - 1)\right] - 1, \qquad (41)$$

$$\mathcal{S} = \frac{2\Lambda^{-1}\xi_0}{\delta^2}\coth\left[\Lambda^{-1}\xi_0\right] - \frac{2}{\delta^2}, \qquad (42)$$

$$\mathcal{T} = -c_{H_2}^0, \qquad (43)$$

$$\mathcal{U} = \left[\frac{\delta^2\Lambda^{-1}(\xi_0 - 1)}{2}\coth\left[\Lambda^{-1}(\xi_0 - 1)\right] - \frac{\delta^2}{2}\right], \qquad (44)$$

$$\mathcal{V} = (\xi_0 - 1)\Lambda^{-1}\coth\left[\Lambda^{-1}\xi_0\right] - 1, \qquad (45)$$

$$\mathcal{W} = c_{O_2}^0. \qquad (46)$$

6 Acknowledgement

Nomenclature

F	Faraday constant, C/mol
R	Gas constant, $J/molK$
T	Temperature, K
C_{ref}	Reference concentration, mol/cm^3
E^{eq}	ORR equilibrium potential, V
H_{H_2}	Henry's law constant for H_2 in Nafion, $mol/cm^3 kPa$
H_{O_2}	Henry's law constant for O_2 in Nafion, $mol/cm^3 kPa$
$D_{H_2}^{nano}$	H_2 diffusion coefficient at nanoscale, cm^2/s
$D_{O_2}^{nano}$	O_2 diffusion coefficient at nanoscale, cm^2/s
$D_{H_2}^{macro}$	H_2 diffusion coefficient at macroscale, cm^2/s
$D_{O_2}^{macro}$	O_2 diffusion coefficient at macroscale, cm^2/s
j_{ORR}^0	ORR exchange current density, A/cm^2
j_{HOR}^0	HOR exchange current density, A/cm^2
$\alpha_{HOR}^a, \alpha_{HOR}^c$	Anodic and cathodic transfer coefficients for HOR
$\alpha_{ORR}^a, \alpha_{ORR}^c$	Anodic and cathodic transfer coefficient for ORR
$p_{H_2}^0$	H_2 pressure at membrane $|$ anode, kPa
$p_{O_2}^0$	O_2 pressure at membrane $|$ cathode, kPa
r_0	Particle radius, nm
n_{pt}	Particle density, μm^{-3}
x	Dimensional coordinate along PEM thickness, μm
l	Membrane thickness, μm
ξ	Dimensionless coordinate along PEM thickness, normalized by PEM thickness
Λ	Dimensionless reaction penetration depth, normalized by PEM thickness

References

1 S. D. Knights, K. M. Colbow, J. St-Pierre and D. P. Wilkinson, *Journal of power sources*, 2004, **127**, 127–134.

2 L. Gubler, S. M. Dockheer and W. H. Koppenol, *Journal of The Electrochemical Society*, 2011, **158**, B755–B769.

3 X. Huang, R. Solasi, Y. Zou, M. Feshler, K. Reifsnider, D. Condit, S. Burlatsky and T. Madden, *Journal of Polymer Science Part B: Polymer Physics*, 2006, **44**, 2346–2357.

4 V. O. Mittal, H. R. Kunz and J. M. Fenton, *Journal of The Electrochemical Society*, 2007, **154**, B652–B656.

5 J. Wu, X. Z. Yuan, J. J. Martin, H. Wang, J. Zhang, J. Shen, S. Wu and W. Merida, *Journal of Power Sources*, 2008, **184**, 104–119.

6 J. Healy, C. Hayden, T. Xie, K. Olson, R. Waldo, M. Brundage, H. Gasteiger and J. Abbott, *Fuel cells*, 2005, **5**, 302–308.

7 P. Ferreira, Y. Shao-Horn, D. Morgan, R. Makharia, S. Kocha, H. Gasteiger *et al.*, *Journal of The Electrochemical Society*, 2005, **152**, A2256–A2271.

8 M. Ghelichi, P.-É. A. Melchy and M. H. Eikerling, *The Journal of Physical Chemistry B*, 2014, **118**, 11375–11386.

9 M. P. Rodgers, B. P. Pearman, L. J. Bonville, D. A. Cullen, N. Mohajeri and D. K. Slattery, *Journal of The Electrochemical Society*, 2013, **160**, F1123–F1128.

10 N. Ohguri, A. Y. Nosaka and Y. Nosaka, *Journal of Power Sources*, 2010, **195**, 4647–4652.

11 L. Ghassemzadeh, K.-D. Kreuer, J. Maier and K. Müller, *The Journal of Physical Chemistry C*, 2010, **114**, 14635–14645.

12 M. Aoki, H. Uchida and M. Watanabe, *Electrochemistry communications*, 2005, **7**, 1434–1438.

13 M. Aoki, H. Uchida and M. Watanabe, *Electrochemistry communications*, 2006, **8**, 1509–1513.

14 A. Ohma, S. Suga, S. Yamamoto and K. Shinohara, *ECS Transactions*, 2006, **3**, 519–529.

15 D. Zhao, B. Yi, H. Zhang and M. Liu, *Journal of Power Sources*, 2010, **195**, 4606–4612.

16 N. Hasegawa, T. Asano, T. Hatanaka, M. Kawasumi and Y. Morimoto, *ECS Transactions*, 2008, **16**, 1713–1716.

17 S. Helmly, B. Ohnmacht, R. Hiesgen, E. Gülzow and K. A. Friedrich, *ECS Transactions*, 2013, **58**, 969–990.

18 N. Macauley, L. Ghassemzadeh, C. Lim, M. Watson, J. Kolodziej, M. Lauritzen, S. Holdcroft and E. Kjeang, *ECS Electrochemistry Letters*, 2013, **2**, F33–F35.

19 N. Macauley, A. S. Alavijeh, M. Watson, J. Kolodziej, M. Lauritzen, S. Knights, G. Wang and E. Kjeang, *Journal of The Electrochemical Society*, 2015, **162**, F98–F107.

20 H. Hagihara, H. Uchida and M. Watanabe, *Electrochimica Acta*, 2006, **51**, 3979–3985.

21 M. P. Rodgers, L. J. Bonville, H. R. Kunz, D. K. Slattery and J. M. Fenton, *Chemical reviews*, 2012, **112**, 6075–6103.

22 T. Madden, D. Weiss, N. Cipollini, D. Condit, M. Gummalla, S. Burlatsky and V. Atrazhev, *Journal of The Electrochemical Society*, 2009, **156**, B657–B662.

23 F. De Bruijn, V. Dam and G. Janssen, *Fuel cells*, 2008, **8**, 3–22.

24 V. Berejnov, Z. Martin, M. West, S. Kundu, D. Bessarabov, J. Stumper, D. Susac and A. P. Hitchcock, *Physical Chemistry Chemical Physics*, 2012, **14**, 4835–4843.

25 W. Bi, G. E. Gray and T. F. Fuller, *Electrochemical and Solid-State Letters*, 2007, **10**, B101–B104.

26 T. Akita, A. Taniguchi, J. Maekawa, Z. Siroma, K. Tanaka, M. Kohyama and K. Yasuda, *Journal of power sources*, 2006, **159**, 461–467.

27 K. Yasuda, A. Taniguchi, T. Akita, T. Ioroi and Z. Siroma, *Physical Chemistry Chemical Physics*, 2006, **8**, 746–752.

28 L. Kim, C. G. Chung, Y. W. Sung and J. S. Chung, *Journal of Power*

Sources, 2008, **183**, 524–532.

29 G. Diloyan, M. Sobel, K. Das and P. Hutapea, *Journal of Power Sources*, 2012, **214**, 59–67.

30 W. Liu and D. Zuckerbrod, *Journal of The Electrochemical Society*, 2005, **152**, A1165–A1170.

31 S. Takaichi, H. Uchida and M. Watanabe, *Electrochemistry communications*, 2007, **9**, 1975–1979.

32 M. Ohishi, Y. Okano, Y. Ono, A. Ohma, K. Fushinobu and K. Okazaki, *International Journal of Heat and Mass Transfer*, 2012, **55**, 7213–7217.

33 V. Atrazhev, N. Erikhman and S. Burlatsky, *Journal of Electroanalytical Chemistry*, 2007, **601**, 251–259.

34 W. Sheng, H. A. Gasteiger and Y. Shao-Horn, *Journal of The Electrochemical Society*, 2010, **157**, B1529–B1536.

35 D. Sepa, M. Vojnovic and A. Damjanovic, *Electrochimica Acta*, 1981, **26**, 781–793.

36 P. D. Beattie, V. I. Basura and S. Holdcroft, *Journal of Electroanalytical Chemistry*, 1999, **468**, 180–192.

37 A. J. Bard and L. R. Faulkner, *Hoboken: Wiley and Sons*, 2001.

38 H. Ju, C.-Y. Wang, S. Cleghorn and U. Beuscher, *Journal of The Electrochemical Society*, 2005, **152**, A1645–A1653.

39 M. M. Mench, *FUEL CELL engines*, John Wiley & Sons, 2008.

40 E. L. Cussler, *Diffusion: mass transfer in fluid systems*, Cambridge university press, 2009.

41 P. Gode, G. Lindbergh and G. Sundholm, *Journal of Electroanalytical Chemistry*, 2002, **518**, 115–122.

42 K. Neyerlin, W. Gu, J. Jorne and H. A. Gasteiger, *Journal of the Electrochemical Society*, 2007, **154**, B631–B635.

43 S. Helmly, R. Hiesgen, T. Morawietz, X.-Z. Yuan, H. Wang and K. A. Friedrich, *Journal of The Electrochemical Society*, 2013, **160**, F687–F697.

44 F. Ettingshausen, J. Kleemann, M. Michel, M. Quintus, H. Fuess and C. Roth, *Journal of Power Sources*, 2009, **194**, 899–907.

45 J. H. Park, H. Zhou, S. J. Percival, B. Zhang, F.-R. F. Fan and A. J. Bard, *Analytical chemistry*, 2013, **85**, 964–970.